International Nano Letters (2021) 11:59–68
https://doi.org/10.1007/s40089-020-00322-w

ORIGINAL ARTICLE

Synthesis and structural characterization of gold nanorods

Paulo Ricardo Abreu Furtado Ricardo Garcia[1] · Wagner Wlysses Rodrigues Araujo[1] · Gabriel Braga Marques Teobaldo[2] · Alan Silva de Menezes[2] · Larissa Otubo[3] · Cristiano Luis Pinto Oliveira[1]

Received: 19 October 2020 / Accepted: 4 December 2020 / Published online: 18 January 2021

Abstract
Gold cylinders with nanometric dimensions were successfully synthesized and characterized by X-ray scattering and diffraction, transmission electron microscopy, dynamic light scattering, and ultraviolet–visible spectroscopy. A small change on the synthesis route led to a slower reaction, allowing better control over the dimensions of the nanorods. The structural characterization enabled the description of the parameters as a function of synthesis time as well as reliable quantification of molar concentrations. The fine-tuning of sizes is crucial for the optimization of the nanorods on specialized applications.

Keywords Gold nanorods · Synthesis · Structural characterization

Introduction

Gold has unique properties in the macro scale, namely, low electrical resistance, protection against oxidation among many other characteristics. However, when going to the nanoscale, particles made of gold, and many other noble materials, also present striking properties which opens a wide range of applications [1, 2]. Gold nanorods (GN) with well-defined sizes can be used as sensors due to their high biocompatibility and unique plasmon resonant properties [3]. In recent applications, GN has been used to enhance chiral recognition of enantiomers [4], drug carriers for photothermotherapy [5], and promote optical information storage [6]. The efficiency of these applications depends on the fine-tuning of the rods' radius and aspect ratios [5]. Therefore, optimized synthesis control and detailed structural characterization of the GN on different synthesis times are crucial for the selection and application of the synthesized nanorods. In this work, a small change in the traditional synthesis procedure led to a synthesis of GN with slower reaction speed and nanorods with a larger radius and smaller aspect ratios when compared to the original synthesis. The structural characterization of the GN was performed using small-angle X-ray scattering, X-ray diffraction, dynamic light scattering, transmission electron microscopy and ultraviolet-visible spectroscopy. As a result, the time evolution of the dimensions of the rods could be followed and described.

Experimental information

Synthesis of the GN

The nanorods were produced using a seed-mediated reduction route. The synthesis is performed in two steps: the preparation of seed and growth solutions. This method was adapted from the one reported in the publication of Morasso et al. [7]. A modification was done in the preparation of the growth solution which made the growth of the nanorods slower. This modification consists of the prior solubilization of a tiny quantity (1 mL) of CTAB aqueous solution with part of the gold solution, thus generating an orange solution. The preparation of the seed and the modified growth solutions are described below.

Electronic supplementary material The online version of this article (https://doi.org/10.1007/s40089-020-00322-w) contains supplementary material, which is available to authorized users.

✉ Cristiano Luis Pinto Oliveira
crislpo@if.usp.br

[1] Instituto de Física, Universidade de São Paulo, Rua do Matão Nr. 1371, Cidade Universitária, São Paulo, SP 05508-090, Brazil

[2] Departamento de Física, CCET, Universidade Federal Do Maranhão, Av. dos Portugueses, 1966, Vila Bacanga, São Luís, MA 65080-805, Brazil

[3] Laboratório de Microscopia E Microanálises (LMM), Instituto de Pesquisas Energéticas E Nucleares, IPEN-CNEN/SP, Avenida Lineu Prestes, 2242, Cidade Universitária, São Paulo, SP 05508-000, Brazil

Seed solution preparation

For the seed solution, cetrimonium bromide (CTAB) is dissolved in MiliQ water at a concentration of 200 mM and was kept at 40 °C under ultrasonication for the complete dissolution of the CTAB. Then, 5 mL of this solution was mixed with 5 mL of a 0.5 mM $HAuCl_4$ aqueous solution at a temperature of 27 °C under ultrasonication. So, 600 µL of $NaBH_4$ (10 mM), previously dissolved in water at 4 °C, was added and the final mixture was kept under vigorous stirring for 20 min.

Modified growth solution preparation

The growth solution was prepared by adding 220 mg hydroquinone (HQ) in 50 mL of a 50 mM CTAB solution at 40 °C under magnetic stirring. After the complete dissolution of the reactants, the temperature was lowered to 27 °C. In parallel, 20 mL of 1 mM $HAuCl_4$ was mixed with 1 mL of the HQ + CTAB solution**.** The color of the solution immediately changed from yellow to orange. Then, the remaining 30 mL of the 1 mM $HAuCl_4$ solution was added to this orange solution. This gold solution was mixed with the remaining 49 mL of the CTAB solution. Then, 2 mL of $AgNO_3$ (4 mM) aqueous solution and 120 µL of the seed solution were added. The final solution had a volume of about 102 mL and was kept at a controlled temperature of 27 °C under vigorous stirring for about 1 h. Then, 8 mL aliquots were collected at different times and immediately cooled in ice to stop the reactions. The aliquots were centrifuged at 10,000 rpm for 10 min. Then the supernatant was extracted leaving only the precipitate. 3 ml of deionized water were added and redispersed.

The color of the sample evolved from dark orange to dark wine (at 60 min synthesis time). The orange color obtained during the synthesis described above may be related to CTAB-$AuCl^{4-}$ interactions. According to Khan et al. [8], when the $HAuCl_4$ and CTAB aqueous solutions are mixed, ion exchanges occurs, forming ion pairs of CTA^+ and $AuCl_4^-$. This reaction occurs under certain concentrations of the CTAB and $HAuCl_4$ [8]. In their work, two orange reaction solutions were obtained: one containing $[HAuCl_4] = 0.2$ mM and $[CTAB] = 0.4$ mM and another containing $[HAuCl_4] = 0.2$ mM and $[CTAB] = 0.6$ mM; corresponding to concentration ratios $[CTAB]/[HAuCl_4] = 2$ and 3. In our work, the orange solution was obtained for $[CTAB] = 2.38$ mM and $[HauCl_4] = 0.95$ mM. It is interesting to note that, even though these CTAB concentrations are much higher than the ones studied by Khan and coauthors, the concentration ratio $CTAB/HauCl_4 = 2.5$, which is in the same range were the same color was obtained in their work.

SAXS measurements

SAXS measurements were performed using a Xeuss 2.0-equipment. The equipment has three X-ray sources (Co, Mo, Cr) and a Pilatus 300 k 2D detector. Several sample-to-detector distances can be mounted, giving a broad range of sample to detector distances, which allows the investigations of sizes from ~ 1 to 400 nm. The scattering intensities are described as a function of the reciprocal space momentum transfer vector $\boldsymbol{q}$, with modulus given by $q = 4\pi\sin(\theta)/\lambda$, where 2θ is the scattering angle and λ the radiation wavelength. In this work, a Cu Kα tube was used ($\lambda = 0.15418$ nm). Two sample sample-to-detector distances were used: 6.5 m and 0.9 m. For 6.5 m one has a q range of $0.025 < q < 0.6$/nm. For 0.9 m the available interval was $0.1 < q < 3.5$/nm. The samples were placed in home-made stainless steel sample holders with glued 1.5 mm glass capillaries and closed with sealing caps. Therefore, the capillaries can be washed and rinsed allowing a proper background subtraction. The 2D scattering data were collected on several frames of 600 s. The images were integrated into 1D curves using the software available in the instrument. The experimental intensity data was treated using standards procedures [9]. Measurement of capillary filled with water was used as background and subtracted from the experimental intensity data. This water sample was also used as a primary standard for absolute scale normalization.

XRD measurements

The samples were characterized by X-ray diffraction by using a laboratory-based equipment Bruker D8 Discover-DaVinci™ equipment equipped with a Cu Kα tube. The measurements were recorded by using a 2θ step of 0.05° and a counting time of 2 s per step, with 2θ varying from 30° to 90°. Due to the low amount of the sample, it was not possible to separate the GN and make powder samples. Instead, drops of the synthesis aliquots were placed on the glass plate and left to dry at ambient temperature. The plates with the deposited thin films were placed on the equipment for measurements on theta-2theta geometry. This thin film procedure was used due to the low volume of the samples, which precluded the production of purified powder samples. The glass plate was rotated at 30 rpm. As shown later, the XRD data showed the presence of gold crystalline structure but the drying process created nonspecific crystal structures of CTAB, making impossible the use of detailed model refinement.

DLS measurements (DLS)

DLS measurements were performed using a Brookhaven 90Plus™ Particle Size Analyzer placed at the Institute of Physics, University of São Paulo. The experimental setup is composed of the laser beam with wavelength 657 nm and the

detector positioned at 90° with respect to the incoming beam. Temporal autocorrelation curves were obtained using standard routines of the acquisition programs. The experiments were performed in homodyne mode. The samples were placed on special plastic cuvettes available at the instrument. The autocorrelation functions were modeled with Non-Negatively Constrained Least Squares (NNLS) method [10]. As a result, size distributions as a function of hydrodynamic sizes were obtained. For the correct interpretation of the obtained hydrodynamic radius and comparison with the other experimental results is necessary to consider the fact that the particles are rods. As shown by Eimer and Pecora [11], the average hydrodynamic radius R_H of a cylinder with diameter d, length L and aspect ratio $p = L/d$, is given by,

$$R_H = L/\left[2(\ln p + \nu)\right] \tag{1}$$

where ν is a polynomial approximation of a numerical simulation for the correction on the translational diffusion coefficient due to the particle anisometry ($2 < \nu < 30$) and is given by [12],

$$\nu = 0.312 + 0.565p^{-1} - 0.100p^{-2} \tag{2}$$

TEM measurements

For registration of transmission electron microscopy (TEM) micrographs, TEM grids were prepared by placing a droplet of sample on the grid without any dilution. The excess of residual GN suspension on the grid was blotted with filter paper, and the grid was allowed to dry at room temperature (~23 °C). Carbon-coated collodion film copper grids were used in this work. Once the TEM grids were prepared, they were mounted and analyzed in a JEOL 2100 TEM Microscope instrument equipped with a LaB_6 filament, a high-resolution (HR) pole piece. The microscope was operated at 200 kV to achieve high-resolution imaging (0.23 nm). Micrographs of ten different regions were registered for each GN sample at a different elapsed time of synthesis. A custom Python 3.6 [13] script was used to perform operations of noise reduction (smooth filter), contrast enhancement, particle segmentation, size (width and length) distributions, and analysis of size distributions. The image processing and segmentation of GN from the background on the TEM micrographs was performed based on Huang's thresholding method [14] implemented in the Scikit-Image [15] library from the Python ecosystem. From the collection of segmented particles, we were able to generate size (width and length) distributions that were stored as data frames in the pandas library [16]. These distributions were fitted to Lognormal distribution [17] by using Scipy library built in the method [18].

Ultraviolet–visible spectroscopy measurements

The ultraviolet–visible spectroscopy (UV–Vis) characterizations were performed using an Ocean Optics USB400 spectrometer and a Mikropack DH-2000-BAL light source. The data were collected in the wavelength range from 178 to 893 nm. The samples were dispersed in a 1 mL water placed in a plastic cuvette.

SAXS modeling

Indirect Fourier transformation (IFT)

The SAXS intensities were modeled with the Indirect Fourier transformation method (IFT) using the Glatter method [19] in a slightly different implementation [20, 21]. As a result, the pair distances distribution function ($p(r)$) is obtained. The shape of the $p(r)$ function gives good indications about the overall particle sizes as well as particle radius of gyration (R_G), maximum size (D_{MAX}), and forward scattering ($I(0)$) [9, 22]. Since the data is normalized to the absolute scale it is possible to estimate the molar concentration of the synthesized GN.

Cylinder model

A theoretical SAXS model describing a system of polydisperse cylinders was also used. The main equation of the model is [23]:

$$I_{rod}(q) = \mathrm{Sc}_{cyl} \int_0^\infty V^2(R,L) P_{cyl}(q,R,L) D(R,\langle R\rangle, z)\, \mathrm{d}R + B \tag{3}$$

where q is the modulus of the momentum transfer vector of the reciprocal space, R is the radius of the cylinder, L is the length of the cylinder, Sc_{rod} is the intensity scale factor, $V(R,L)$ is the volume of the cylinder, $P_{cyl}(q,R,L)$ is cylinders form factor, $D(R,\langle R\rangle, z)$ is the radius distribution function and B is the background. The full expression of the cylinders form factor is:

$$P_{cyl}(q,R,L) = \int_0^{\pi/2} \left[\frac{2J_1(qR\sin\alpha)}{qR\sin\alpha} \frac{\sin(qL\cos\alpha/2)}{qL\cos\alpha/2}\right]^2 \sin\alpha\, \mathrm{d}\alpha \tag{4}$$

J_1 is the Bessel function of the first kind.

The radius distribution $D(R, <R>, z)$ was modeled using a Schulz–Zimm function [23]:

$$D(R,\langle R\rangle,z)=\left(\frac{z+1}{\langle R\rangle}\right)\frac{R^z}{\Gamma(z+1)}\exp\left(-(z+1)\frac{R}{\langle R\rangle}\right) \quad (5)$$

$$\int_0^\infty D(R,R,z)\,\mathrm{d}R=1 \quad (6)$$

where $<R>$ is the average radius, $z=1/(\sigma/<R>)^2$ and σ is the standard deviation of the distribution.

Core–shell ellipsoids of revolution

The scattering intensity of the CTAB micelles was described using a form factor of core–shell ellipsoids of revolution [23]. The SAXS intensity data of the CTAB samples indicated a strong structure factor interaction among the micelles. For simplicity, this interaction was included in the model by the use of a hard sphere structure factor $S_{\mathrm{HS}}\left(q,R_{\mathrm{HS}},\eta\right)$ [24]. The whole model is written as:

$$I_{\mathrm{mic}}(q)=\mathrm{Sc}_{\mathrm{mic}}\left[\int_0^\infty P_{\mathrm{mic}}\left(q,R_{\mathrm{C}},T,\epsilon\right)D\left(R_{\mathrm{C}},\langle R_{\mathrm{C}}\rangle,\sigma_{\mathrm{C}}\right)\mathrm{d}R_{\mathrm{C}}\right]S_{\mathrm{HS}}\left(q,\eta,R_{\mathrm{HS}}\right)+B \quad (7)$$

where R_{C} is the radius of the core, T is the shell thickness, ϵ is ellipsoid anisotropy (for spheres $\epsilon=1$, prolate ellipsoids have $\epsilon>1$ and oblate ellipsoids $\epsilon<1$), RHS is the hard sphere interaction radius, η is the hard sphere volume fraction and $P_{\mathrm{mic}}\left(q,R_{\mathrm{C}},T,\epsilon\right)$ is the a form factor of the core–shell ellipsoids of revolution:

$$P_{\mathrm{mic}}\left(q,R_{\mathrm{C}},T,\epsilon\right)=\int_0^{\pi/2}F_{\mathrm{CS}}\left[q,r\left(R_{\mathrm{C}},\epsilon,\alpha\right),T\right]^2\sin\alpha\,\mathrm{d}\alpha \quad (8)$$

where $r\left(R_{\mathrm{C}},\epsilon,\alpha\right)=R_{\mathrm{C}}\sqrt{\sin^2\alpha+\epsilon\cos^2\alpha}$ and the modulus of the core–shell scattering amplitude $F_{\mathrm{CS}}(q,R,T)$ is given by:

$$F_{\mathrm{CS}}(q,R_{\mathrm{C}},T)=\frac{\Delta\rho_{\mathrm{shell}}}{\Delta\rho_{\mathrm{core}}}(V_{\mathrm{core}}+V_{\mathrm{shell}})F_{\mathrm{sph}}\left(q,R_{\mathrm{C}}+T\right)+\left(1-\frac{\Delta\rho_{\mathrm{shell}}}{\Delta\rho_{\mathrm{core}}}\right)V_{\mathrm{core}}F_{\mathrm{sph}}\left(q,R_{\mathrm{C}}\right) \quad (9)$$

$F_{\mathrm{sph}}\left(q,R_{\mathrm{C}}\right)$ is the modulus of the scattering amplitude of a sphere, V_{core} and V_{shell} are the volumes of the core and shell, respectively. $\frac{\Delta\rho_{\mathrm{shell}}}{\Delta\rho_{\mathrm{core}}}$ is the ratio between the electron density contrast of the shell and the core. R_{C} is the radius of the core and T is the thickness of the shell.

GN and CTAB micelles

For the SAXS data at 1.2 m the presence of the CTAB micelles is visible at the scattering curves and therefore is necessary to include it in the final intensity. This is done by a simple combination of the intensity of the cylinders and core–shell micelles, however, considering SHS(q, η, RHS)=1 since the effects of the interactions among the micelles are not apparent in these SAXS curves:

$$I(q)=I_{\mathrm{rod}}(q)+I_{\mathrm{mic}}(q) \quad (10)$$

Estimation of GN molar concentration

The forward scattering of a system composed of particles with volume V, electron density ρ_{GN}, dispersed in a medium with electron density ρ_{sol} and molar concentration c_{M} is given by [9]:

$$I(0)_{\mathrm{GN}}=\frac{c_{\mathrm{M}}N_{\mathrm{A}}}{1000}\left(\rho_{\mathrm{GN}}-\rho_{\mathrm{sol}}\right)^2r_0^2V^2\left[\mathrm{cm}^{-1}\right] \quad (11)$$

where N_{A} is the Avogadro's number and r_0 is the classical radius of the electron. Assuming that the GN are formed by crystalline gold and dispersed in water, the electron density contrast is $\Delta\rho_{\mathrm{GN}}=\rho_{\mathrm{GN}}-\rho_{\mathrm{sol}}=4.324\frac{\mathrm{el}}{\mathrm{Å}^3}$. In the above expression, the volume is expressed in cm^3 and r_0 in cm. Therefore, the molar concentrations of the GN is given by (Fig. 1):

$$c_{\mathrm{M}}=\frac{1000I(0)_{\mathrm{GN}}}{N_{\mathrm{A}}\Delta\rho_{\mathrm{GN}}^2r_0^2V^2}[\mathrm{mol/L}] \quad (12)$$

Results and discussion

GN produced using the modified synthesis route

The experimental investigations were performed on the centrifuged and redispersed aliquots. Figure 1a shows the SAXS data collected. Interesting, a visual inspection reveals that the intensity profiles show a very well-defined Guinier region, where the slope of the intensity curves in log–log scale tends to zero for low q values [25]. Also, the curves display a prominent oscillation at $q\approx0.29$/nm, which is an

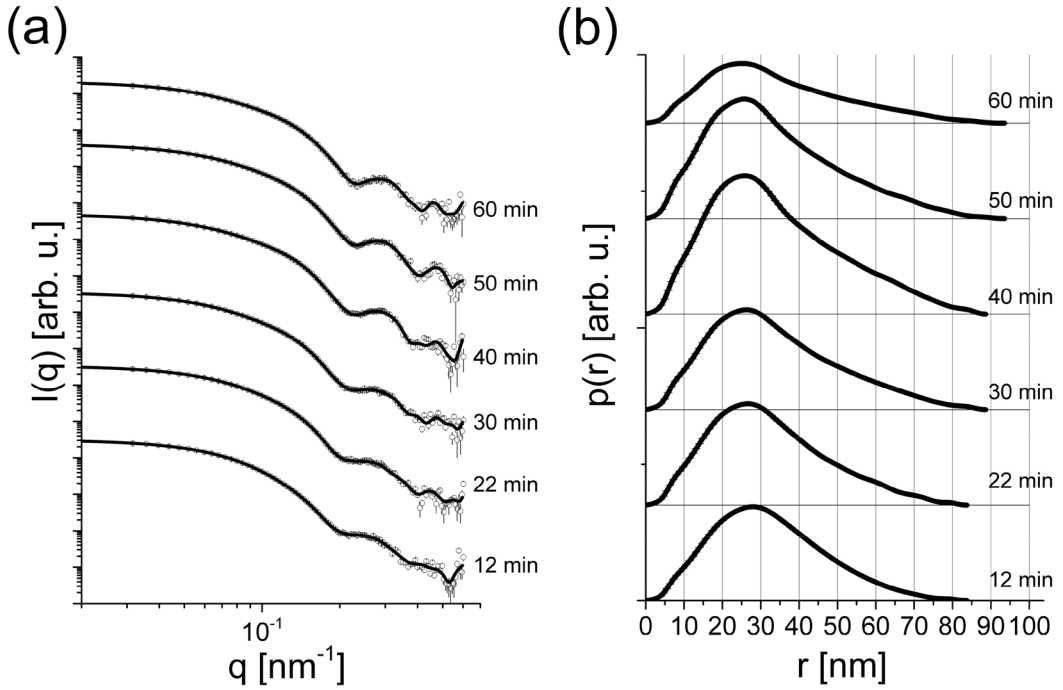

Fig. 1 SAXS intensity data. **a** Experimental data (symbols) and theoretical curve (full line) calculated using the IFT procedure. **b** Obtained $p(r)$ curves

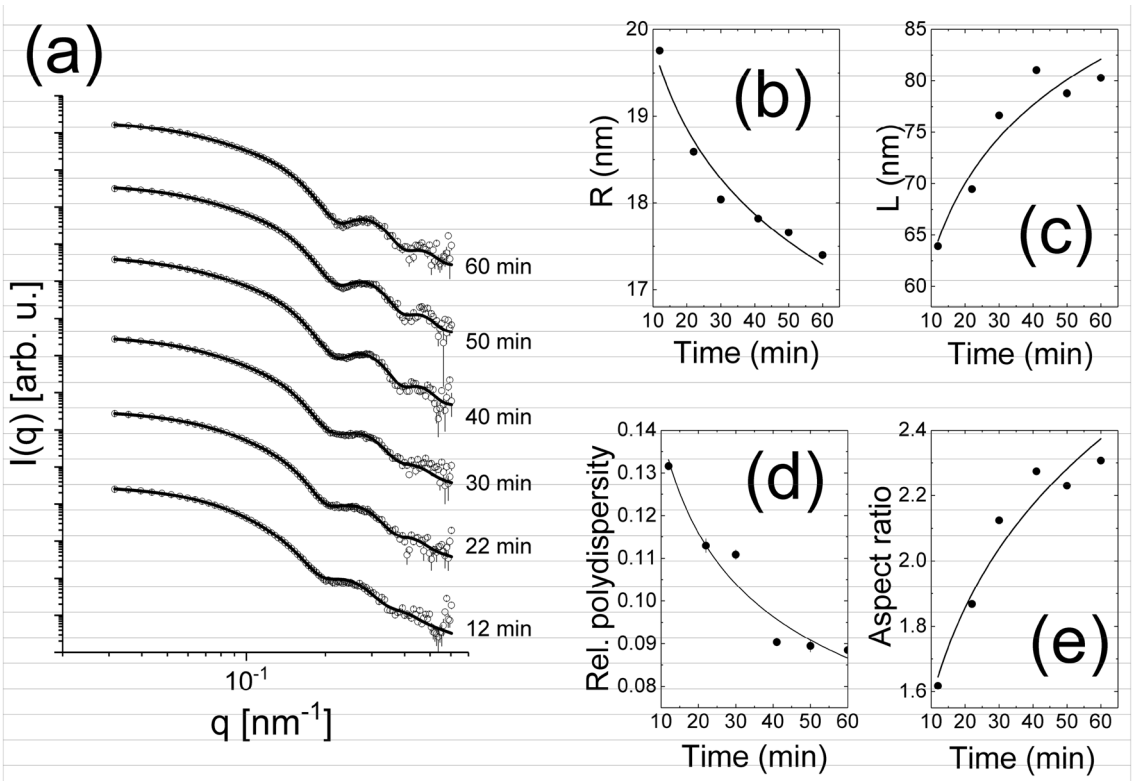

Fig. 2 SAXS modeling results. **a** SAXS experimental data (symbols) and theoretical curve (full line) calculated using a model of polydisperse cylinders. Temporal evolution of SAXS structural parameters: **b** average radius, **c** average length, **d** relative polydispersity (σ/R) of the system and **e** aspect ratio ($L/2R$). Solid lines in **b**–**e** are trend lines

indication of relatively low polydispersity. Figure 1b shows the obtained pair distances distribution functions $p(r)$ for the collected SAXS data. The shape of the $p(r)$ curves are typical for rod-like particles. The values where the curves go to zero indicates the maximum dimensions of the nanoparticles. Also, the point of inflexion of the curves just after the maximum is a rough indication of the particle diameter [26]. Monodisperse cylinders have a linear descent of the $p(r)$ curves after the point of inflexion. In the present case, this descent is not perfectly linear due to a small polydispersity in sizes, as demonstrated by the modeling of the data using theoretical form factor [26]. Even though the system is not perfectly monodisperse, the IFT method provides a good indication of the average sizes and shapes. Interestingly, a small shoulder is also seen in the $p(r)$ curves around ~ 10 nm. This may come from the presence of free CTAB micelles in the system and also from the CTAB molecules around the GN. CTAB micelles have a high affinity to gold surfaces, as demonstrated by molecular dynamic simulations [27], and are crucial for the stabilization of the GN in the solution. The structural parameters obtained from IFT are shown in Table 1. From the forward scattering values, $I(0)$, it is possible to estimate the molar concentrations, given the particle volumes, as shown later in the text.

The model fits using the theoretical form factor of polydisperse cylinders is shown in Fig. 2a. The good agreement between the model and experimental data indicate that the system is well described as cylinders. This oscillation becomes more pronounced as the synthesis time increases, suggesting that the polydispersity of the system decreases with time.

The theoretical model of polydisperse cylinders (Eq. 1) was used to describe the experimental SAXS data. The temporal evolution of the average radius, length, and polydispersity, determined using the SAXS modeling, are shown in Table 2 and Fig. 2a–c. The relative polydispersity in radius is calculated and used for the length in an affine approximation. The average radius of the cylinders presents a decrease with time. The average length, on the other hand, shows the tendency to grow, leading to an increase in the aspect ratio, as shown in Fig. 2d. These results suggest that the GN becomes more elongated while the growth rate decreases with synthesis time. The relative polydispersity curve (σ/R), shown in Fig. 2c, reveals that the system becomes less polydisperse during the synthesis time.

The DLS results are shown in Fig. 3. The correlation curves shown in (a) are characteristic of a system with two main contributions. By using the NNLS model one can obtain the intensity size distributions, shown in (b). One can see well-defined maximums in these plots. The first one at ~ 6–7 nm is related to the CTAB micelles in the system. The other maximum, at ~ 70 nm is from the GN. In all synthesis times, the presence of the two maximums indicates the presence of CTAB micelles and GN during the whole synthesis. The position of the second maximum stays approximately at the same position until 50 min. For 60 min a third maximum appeared at around ~ 350 nm. This can indicate the presence of tiny fractions (< 0.001% in volume fraction) of large aggregates in the system, which is likely a dust particle in the system. The third peak seems to make the second maximum, related to the GN, to move to lower values in the NNLS optimization (probably an artifact of the modeling method). From the peak position of the second maximum, it is possible to obtain the average hydrodynamic radius RH for the GN. The values are shown in Table 3.

The TEM images of the aliquots, shown in Fig. 4, reveals GN with well-defined shapes and relatively low polydispersity. The calculus of the average sizes, displayed in Table 4, based on the images shows a tendency to increase the sizes with time. From the GN dimensions, one can estimate the hydrodynamic radius R_H, using Eq. (1). Calculations using the dimensions obtained from SAXS and TEM indicated that the TEM dimensions provide R_H values closer to the DLS results. This can indicate that the sizes obtained from the micrographs were influenced by the CTAB shell around the GN. Since Au has a much larger electron density than the surfactants, the SAXS data mostly show the gold core dimensions and not the CTAB contributions. Interestingly,

Table 1 Structural parameters for the GN as a function of synthesis time

Time (min)	Rg (nm)	sRg (nm)	I(0) (/cm)	sI(0) (/cm)
12	25.42	0.03	31.14	0.04
22	25.59	0.03	33.75	0.03
30	26.87	0.03	34.99	0.05
40	27.21	0.02	49.27	0.04
50	26.81	0.04	41.39	0.05
60	27.39	0.05	21.28	0.04
12	25.42	0.03	31.14	0.04

Table 2 Structural parameters calculated using the theoretical SAXS model

	12 min	22 min	30 min	40 min	50 min	60 min
Sc	29.1 (1)	23.0 (1)	25.2 (1)	33.8 (1)	29.79 (1)	19.91 (8)
R (nm)	19.76 (3)	18.60 (2)	18.04 (2)	17.82 (1)	17.66 (2)	17.45 (2)
σ (nm)	2.60 (2)	2.10 (3)	1.99 (2)	1.61 (1)	1.58 (2)	1.54 (1)
L (nm)	63.9 (3)	69.5 (3)	76.6 (4)	81.1 (3)	78.8 (4)	80.3 (4)

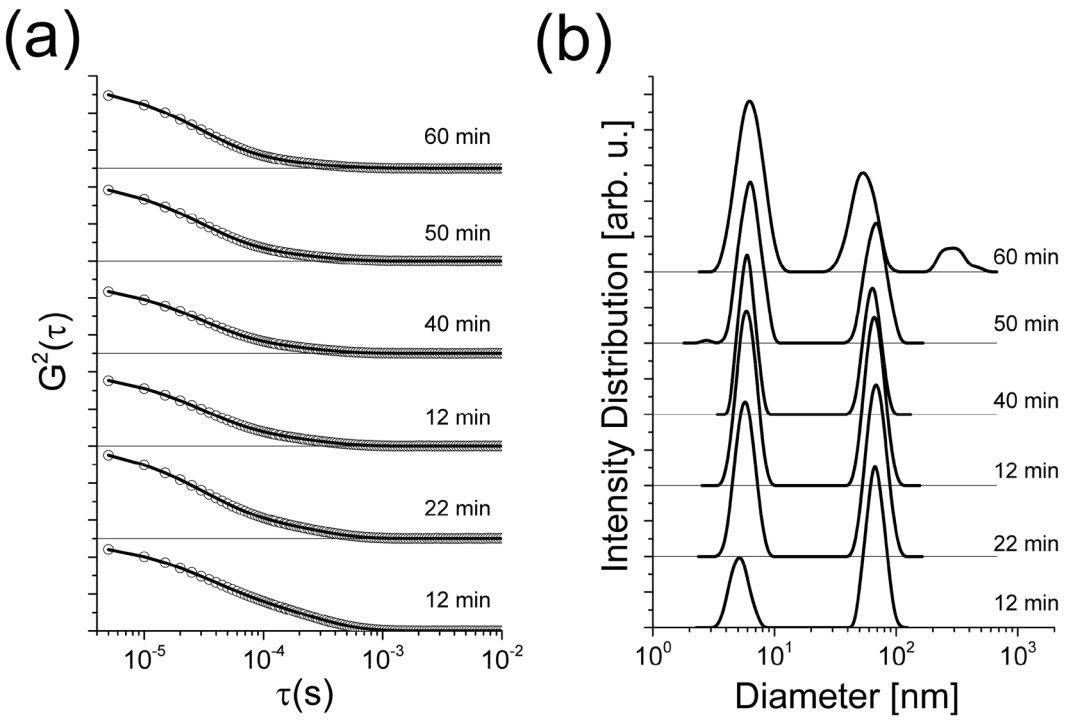

Fig. 3 DLS data. **a** Experimental data (symbols) and NNLS model fit (full line). **b** Distribution of diameters weighted by intensity

Table 3 Hydrodynamic radius obtained from DLS experiments

	10 min	22 min	30 min	41 min	50 min	60 min
R_H (nm)	33.3	33.8	33.3	31.9	34.3	27.5[a]

[a]Value underestimated. See text

the values are shown in Tables 3 and 4 show a very nice agreement between the results of the hydrodynamic radius R_H.

The UV–Vis results are shown in Figure S2. The shape of the UV–Vis curves presents two maximums, which is a characteristic feature of anisotropic particles as GN, where one can have transversal and longitudinal surface plasmon resonance (LSPR) bands. The maximum at ~ 525 nm is related to the particle diameter and the other maximum at larger wavelengths is related to the length of the GN. As time evolves, one can see a systematic movement of the second maximum from ~ 600 up to ~ 750 nm, which is an indication that the length of the GN is increasing.

The aspect ratio ($L/2R$) is frequently analyzed in publications about GN [28–31]. Usually, the values reported for the synthesis route reported by Morasso et al. [7] range from ~ 2 to 3.5. For visual inspection of the overall synthesis behavior, in Figure S1 are shown photos of the unchanged synthesis reactor at different times. The liquid has a characteristic color for Au colloids, getting darker over time, which indicates the growth of the GN. The SAXS results for aliquots taken at the end of the synthesis route are shown in Figure S2 and Table S1, showing an aspect ratio of ~ 2.93. The small change in the synthesis route described above promotes the formation of wider GN. Figure 2e shows the evolution of the aspect ratio calculated using SAXS data, the values obtained vary from ≈ 1.6 to 2.4. A tentative description of the contribution of CTAB micelles to the SAXS curves is shown in "Supplementary Information" (Figure S3). This investigation was also made for the unchanged synthesis route. The obtained micelle sizes and characteristics are similar to previous results present in the literature [32]. Since the lengths of cylinders cannot be accessed for used SAXS setup (0.9 m), the lengths of the cylinders were set to 60 nm, as indicated by the USAXS data for the unchanged synthesis (Table S1). The modeling of the SAXS data demonstrated that the centrifugation of the samples decreases the concentration of the micelles in the system (Table S2). However, the stability of the GN after centrifugation is decreased [33]. The cylinder's diameter and polydispersity for the SAXS and USAXS data are not identical because they correspond to different synthesis batches of the unchanged synthesis. However, the results show the same trend, which indicates a nice reproducibility of the synthesis.

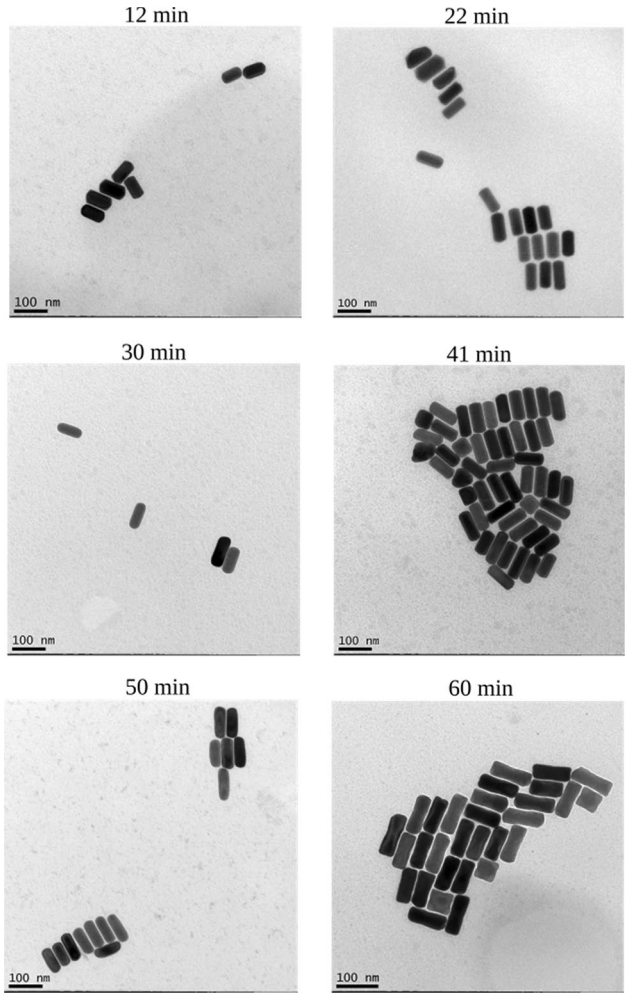

Fig. 4 TEM images of GN aliquots taken at different synthesis time

The aspect ratio can be compared to the position of the second maximum of the UV–Vis spectra, shown in Figure S4. There is a number of papers in the literature investigating the relationship between these two parameters since, in theory, it would allow an easy determination of the aspect ratio by just measuring the absorbance UV–Vis spectra, which is a relatively simple experiment. Several studies demonstrate an approximately linear dependence between the aspect ratio and the LSPR band [28, 29, 31].

Aspect ratios are usually calculated using TEM data. However, as mentioned above, the sizes from TEM images somewhat includes the CTAB shell, making the dimensions from TEM larger than the ones obtained from SAXS data, since SAXS mostly 'sees' the core of the GN. Also, the sampling promoted on SAXS experiments is much larger than the one in TEM analysis. One can check the comparison between the position of the longitudinal LSPR band λ_{max} and the aspect ratio calculated using both SAXS and TEM data. For this comparison, λ_{max} was plotted as a function of the aspect ratio, as it is shown in Fig. 5. Indeed, the points seem to follow a linear trend with a similar slope but different linear coefficients. The linear relations obtained from the fits are given by:

$$\text{SAXS: } \lambda_{\text{Max}} = (400 \pm 30) + (140 \pm 14) \times (L/2R) \tag{13}$$

$$\text{TEM: } \lambda_{\text{Max}} = (400 \pm 30) + (130 \pm 13) \times (L/2R) \tag{14}$$

The XRD data for several aliquots is shown in Figure S5. In the diffractograms, it is possible to see a series of peaks, corresponding to several phases in the system. Comparing the peaks of the XRD pattern of Au face-centered-cubic lattice (JCPDS no. 04-0784) it is possible to identify the presence of crystalline gold in the system, which indicates that the GN has a well-defined crystalline structure. The other peaks are related to the unspecific crystallization of the CTAB content during the measurements. Even though it is not possible to perform a detailed quantitative analysis of the XRD data, the results indicate the formation of crystalline GN. A systematic investigation of XRD data for optimized sample conditions would provide more details on the structure of the GN and will be investigated in future works.

Conclusions

In this work, a systematic investigation of GN synthesis was performed. By using a combination of several experimental techniques, it was possible to obtain a detailed structural characterization of the nanoparticles in the system.

Table 4 Structural parameters calculated using the TEM images

	10 min	22 min	30 min	41 min	50 min	60 min
R (nm)	21.5	20.7	18.4	20.6	17.7	19.9
L (nm)	76.5	85.5	80.4	96.6	86.1	101.2
σ_R (nm)	1.9	1.9	2.9	1.0	2.5	0.8
σ_L (nm)	7.6	6.8	13.6	5.8	7.7	6.1
R_H[a]	32.6	33.2	30.2	34.8	34.8	34.8

[a]Estimated from cylinders dimensions using Eq. (1)

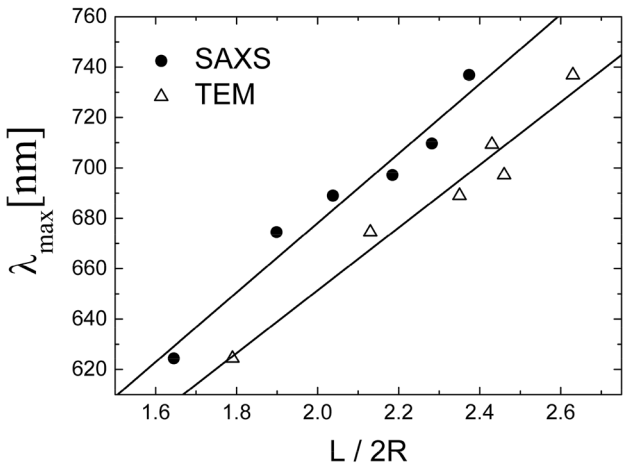

Fig. 5 Position of the longitudinal LSPR band (λ_{max}) versus the aspect ratio calculated using the SAXS data (solid circles) and TEM (open triangles). Full lines are linear fits for each dataset

A small change on a previously published synthesis route promoted an important variation on the aspect ratio of the GN. Well-defined GN were obtained, with diameters of ~ 35–40 nm and lengths of ~ 70–90 nm. The aspect ratio of the GN is a very important parameter since the sizes are related to plasmon resonant frequencies which, on the other hand, influences its use in technological applications.

The comparison of the results for the unchanged and changed synthesis indicates that the GN in the changed synthesis route has a larger diameter and shorter aspect ratios. This indicates that the reaction initiated by the separated solution of CTAB and $HAuCl_4$, as described in the previous sections, leads to shorter aspect ratios. Sau and Murphy [34] investigated several aspects of the GN synthesis and concluded that the production of shorter rods can be obtained by decreasing the overall CTAB concentration in the solution but the production yield drops and non-rod particles are generated. The change proposed in this work open other possibilities for the synthesis of GN in a broader range of aspect ratios and, expanding its applicability. For example, mixtures of GN with two well-defined sizes can be used as a resonator for two defined wavelengths. However, the use of GN demands a precise quantification of the concentration in the system since. In this work, we present a procedure for estimation of the molar concentration based on the use of SAXS data. As shown in the text, for the synthesis of GN, typical concentrations of ~ pM were obtained which, in other words, indicates concentrations of ~ 2000–5000 GN mm^3. The results presented in this work can be used to optimize the production and quantification of GN.

Acknowledgements This work was supported by Fundação de Amparo à Pesquisa do Estado de São Paulo (FAPESP-2018/16092-5, 2016/24531-3), Conselho Nacional de Desenvolvimento Científico e Tecnológico (CNPq-303001/2019-4) e Instituto Nacional de Ciência e Tecnologia em Fluidos Complexos, INCT-FCx.

References

1. Cobley, C.M., Chen, J.Y., Cho, E.C., Wang, L.V., Xia, Y.N.: Gold nanostructures: a class of multifunctional materials for biomedical applications. Chem. Soc. Rev. **40**(1), 44–56 (2011)
2. Shnoudeh, A.J., Hamad, I., Abdo, R.W., Qadumii, L., Jaber, A.Y., Surchi, H.S., et al.: Chapter 15—synthesis, characterization, and applications of metal nanoparticles. In: Tekade, R.K. (ed.) Biomaterials and Bionanotechnology, pp. 527–612. Academic Press, Cambridge (2019)
3. Rao, H.H., Xue, X., Wang, H.Q., Xue, Z.H.: Gold nanorod etching-based multicolorimetric sensors: strategies and applications. J. Mater. Chem. C. **7**(16), 4610–4621 (2019)
4. Wang, Y.W., Zhou, X.J., Xu, C.L., Jin, Y., Li, B.X.: Gold nanorods as visual sensing platform for chiral recognition with naked eyes. Sci. Rep. **8**, 1–9 (2018)
5. Meng, L.Q., Zhang, J.S., Li, H.Q., Zhao, W.W., Zhao, T.G.: Preparation and progress in application of gold nanorods. J. Nanomater. **2019**. Article ID 4925702, 11 pages (2019)
6. Chon, J.W.M., Bullen, C., Zijlstra, P., Gu, M.: Spectral encoding on gold nanorods doped in a silica sol–gel matrix and its application to high-density optical data storage. Adv. Func. Mater. **17**(6), 875–880 (2007)
7. Morasso, C., Picciolini, S., Domitilla, S., Mehn, D., Ojea-Jimenez, I., Zanchetta, G., et al.: Control of size and aspect ratio in hydroquinone-based synthesis of gold nanorods. J. Nanoparticle Res. **17**:330, 1–7 (2015)
8. Khan, Z., Singh, T., Hussain, J.I., Hashmi, A.A.: Au(III)-CTAB reduction by ascorbic acid: preparation and characterization of gold nanoparticles. Colloids Surfaces B-Biointerfaces. **104**, 11–17 (2013)
9. Oliveira, C.L.P.: Investigating macromolecular complexes in solution by small angle X-ray scattering. In: Chandrasekaran, D.A. (ed.) Current Trends in X-ray Crystallography, pp. 367–392. InTech, London (2011)
10. Ross, D.A., Dimas, N.: Particle sizing by dynamic light-scattering—noise and distortion in correlation data. Part. Part. Syst. Char. **10**(2), 62–69 (1993)
11. Eimer, W., Pecora, R.: Rotational and translational diffusion of short rodlike molecules in solution—oligonucleotides. J. Chem. Phys. **94**(3), 2324–2329 (1991)
12. Tirado, M.M., Martinez, C.L., Delatorre, J.G.: Comparison of theories for the translational and rotational diffusion-coefficients of rod-like macromolecules—application to short DNA fragments. J. Chem. Phys. **81**(4), 2047–2052 (1984)
13. Van Rossum, G., Drake, F.L.: Python 3.6 Reference Manual. CreateSpace, Scotts Valley (2009)
14. Huang, L.K., Wang, M.J.J.: Image thresholding by minimizing the measures of fuzziness. Pattern Recogn. **28**(1), 41–51 (1995)
15. van der Walt, S., Schonberger, J.L., Nunez-Iglesias, J., Boulogne, F., Warner, J.D., Yager, N., et al.: scikit-image: image processing in Python. Peerj. **2**, e453 (2014)
16. McKinney, Wa.: Python for Data Analysis: Data Wrangling with Pandas, NumPy, and IPython, 2nd edn. O'Reilly Media. ISBN: 9789351100065
17. Garcia, P., Prymak, O., Grasmik, V., Pappert, K., Wlysses, W., Otubo, L., et al.: An in situ SAXS investigation of the formation of silver nanoparticles and bimetallic silver–gold nanoparticles in

controlled wet-chemical reduction synthesis. Nanosc. Adv. **2**(1), 225–238 (2020)
18. Virtanen, P., Gommers, R., Oliphant, T.E., Haberland, M., Reddy, T., Cournapeau, D., et al.: SciPy 1.0: fundamental algorithms for scientific computing in Python. Nat. Methods. **17**(3), 261–272 (2020)
19. Glatter, O.: New method for evaluation of small-angle scattering data. J. Appl. Crystallogr. **10**(OCT1), 415–421 (1977)
20. Pedersen, J.S.: Model-independent determination of the surface scattering-length-density profile from specular reflectivity data. J. Appl. Crystallogr. **25**, 129–145 (1992)
21. Oliveira, C.L.P., Behrens, M.A., Pedersen, J.S., et al.: A SAXS study of glucagon fibrillation. J. Mol. Biol. **387**(1), 147–161 (2009)
22. Glatter, O.: Determination of particle-size distribution-functions from small-angle scattering data by means of the indirect transformation method. J. Appl. Crystallogr. **13**(1), 7–11 (1980)
23. Lindner, P., Zemb, T.: Neutrons, X-rays and Light: Scattering Methods Applied to Soft Condensed Matter. Elsevier, Amsterdam (2002)
24. Kinning, D.J., Thomas, E.L.: Hard-sphere interactions between spherical domains in Diblock copolymers. Macromolecules **17**(9), 1712–1718 (1984)
25. Guinier, A., Fournet, G., Yudowitch, K.L.: Small-angle scattering of X-rays. New York, Wiley (1955)
26. Glatter, O., Kratky, O.: Small Angle X-ray Scattering. Academic Press, London (1982)
27. da Silva, J.A., Dias, R.P., da Hora, G.C.A., Soares, T.A., Meneghetti, M.R.: Molecular dynamics simulations of cetyltrimethylammonium bromide (CTAB) micelles and their interactions with a gold surface in aqueous solution. J. Braz. Chem. Soc. **29**(1), 191–199 (2018)
28. Pelton, M., Aizpurua, J., Bryant, G.: Metal-nanoparticle plasmonics. Laser Photonics Rev. **2**(3), 136–159 (2008)
29. Encina, E.R., Coronado, E.A.: Resonance conditions for multipole plasmon excitations in noble metal nanorods. J. Phys. Chem. C. **111**(45), 16796–16801 (2007)
30. Amendola, V., Pilot, R., Frasconi, M., Maragò, O.M., Iatì, M.A.: Surface plasmon resonance in gold nanoparticles: a review. J. Phys. Condensed Matter. **29**(20), 203002 (2017)
31. Eustis, S., El-Sayed, M.A.: Determination of the aspect ratio statistical distribution of gold nanorods in solution from a theoretical fit of the observed inhomogeneously broadened longitudinal plasmon resonance absorption spectrum. J. Appl. Phys. **100**(4), 044324 (2006)
32. Goyal, P.S., Dasannacharya, B.A., Kelkar, V.K., Manohar, C., Rao, K.S., Valaulikar, B.S.: Shapes and sizes of micelles in ctab solutions. Phys. B **174**(1–4), 196–199 (1991)
33. Garcia, P.R.A.F.: Rotas de síntese e métodos de caracterização estrutural para sistemas de nanopartículas metálicas. Universidade de São Paulo, São Paulo (2020)
34. Sau, T.K., Murphy, C.J.: Seeded high yield synthesis of short Au nanorods in aqueous solution. Langmuir **20**(15), 6414–6420 (2004)